Key Points:
- Imaging weak localized change within scattering medium
- Numerical computation of the sensitivity kernel in general medium
- Resolution depends on traveltime, scattering medium, and source-receiver setup

Correspondence to:
C. Kanu,
ckanu@mines.edu

Time-lapse imaging of a localized weak change with multiply scattered waves using numerical-based sensitivity kernel

Chinaemerem Kanu[1] and Roel Snieder[1]

[1]Center for Wave Phenomena, Department of Geophysics, Colorado School of Mines, Golden, Colorado, USA

Abstract Multiply scattered seismic waves, due to their long path length within a finite volume, provide information that can be used to detect and image weak time-lapse changes within a medium. Such weak changes are usually not resolved with singly scattered waves. Previous use of multiply scattered waves for time-lapse monitoring assume statistical homogeneity of the scattering property of the scattering medium. This homogeneity is usually characterized by either a constant mean free path or a diffusion coefficient. In a realistic medium, however, this assumption of homogeneity likely breaks down. We demonstrate the capability of resolving a localized time-lapse velocity change within a three-layer 2-D scattering model using multiply scattered waves. The layers within the model have different scattering properties. The imaging algorithm requires numerically generating the sensitivity kernel that correctly represents the statistical heterogeneity of the scattering model. We localize the weak velocity change, but the resolution of the imaged change degrades with increasing coda traveltime. A comparison of the imaged changes from the numerical kernel and the kernel that assumes statistical homogenous model suggests that the numerical kernel provides a stronger constraint on the shape of the imaged velocity change.

1. Introduction

Various monitoring tools have been developed to monitor and characterize weak changes within a wide spectrum of media which includes the Earth's subsurface, mechanical structures such as buildings, and medical specimens. These monitoring tools range from single-scattering wave methods (such as sonic/seismic tomography [*Lumley*, 2001; *Nolet*, 1987], reflection/transmission methods [*Daley et al.*, 2008], and time-lapse microscopy [*Landrø*, 2001]) to multiply scattered wave methods (such as diffusion (acoustic) wave spectroscopy (D(A)WS) [*Pine et al.*, 1988; *Cowan et al.*, 2002] and coda wave interferometry (CWI) [*Snieder et al.*, 2002; *Snieder*, 2006]). The strengths and limitations of these monitoring tools depend on the sensitivity of the monitoring data to the change in the medium. It has been demonstrated that multiply scattered waves are more likely to identify weak temporal changes than do single-scattered waves [*Grêt et al.*, 2006; *Larose and Hall*, 2009]. Multiply scattered waves, due to increased scattering, provide information about the monitored medium that can be used to increase the resolution of the imaged medium [*Belkebir et al.*, 2006], increase illumination especially within poorly illuminated subsurface [*Gaburro et al.*, 2007], and increase the detection of weak time-lapse changes within the medium [*Poupinet et al.*, 1984]. The increased detectability of the weak changes can be seen when compared to monitoring weak changes with singly scattered waves. However, because of the averaging of multiply scattered waves in random scattering media and the complexity in the travel paths of the multiply scattered waves, the spatial resolution of the weak changes is usually not high compared to the resolution provided by singly scattered waves.

Initial efforts in using multiply scattered waves for time-lapse monitoring were successfully used for detecting changes within a monitored medium [*Poupinet et al.*, 1984; *Nishimura et al.*, 2000; *Snieder et al.*, 2002; *Wegler and Sens-Schönfelder*, 2007]. Techniques like D(A)WS and CWI are geared toward measuring global change within a medium thereby averaging the changes present across the monitored medium regardless of whether the changes are localized or not. However, imaging the locations of weak time-lapse changes was a focus of recent research [*Rossetto et al.*, 2011; *Obermann et al.*, 2013a; *Planès et al.*, 2014]. The first known recipe for inverting a localized change using multiply scattered waves is given by *Pacheco and Snieder* [2005] who relate the mean traveltime changes to a localized slowness change. *Larose et al.* [2010] and *Rossetto et al.* [2011] introduce a technique, called LOCADIFF, which uses the decorrelation of the time-lapse scattered waves to image a localized change in the scattering medium. These efforts at localizing changes within a scattering medium assume statistically homogeneous scattering models. How well these methods resolve weak

changes in complex heterogeneous media especially in media where the scattered waves have nondiffusive behavior is unknown.

In this study we investigate the capability of imaging a localized weak velocity change within a scattering medium with heterogeneous statistical scattering properties. Using a numerical example of structurally heterogeneous model, we demonstrate the use of traveltime changes and numerically generated sensitivity kernel to image a localized time-lapse velocity change embedded within the heterogeneous medium. Section 2 provides a brief theoretical summary of the imaging problem. Section 3 explores the averaging effect of multiply scattered waves within a random scattering model and the spatial broadening of multiply scattered waves with increase in traveltime. In section 4, we provide an algorithm to image a localized velocity change within a statistically heterogeneous medium using numerically generated sensitivity kernels. We also, in section 4, compare the imaged velocity change using either the numerical or the analytical kernels and describe how the resolution of the imaged change in the model depends on the spatial broadening of the sensitivity kernel and on the averaging out of the estimated fractional velocity change with increase in traveltime.

2. Theory

Pacheco and Snieder [2005] developed a sensitivity kernel $K(\mathbf{s}, \mathbf{x_o}, \mathbf{r}, t)$ that is based on the intensity of multiply scattered waves which relates mean traveltime changes $\langle \tau(t) \rangle$ to a localized relative velocity change $\delta v / v(\mathbf{x_o})$ at $\mathbf{x_o}$:

$$\langle \tau(t) \rangle = - \int_V K\left(\mathbf{s}, \mathbf{x_o}, \mathbf{r}, t\right) \frac{\delta v}{v}(\mathbf{x_o}) \, dV(\mathbf{x_o}), \tag{1}$$

where V is the scattering volume and $\mathbf{s}$ and $\mathbf{r}$ are the source and the receiver locations, respectively. We estimate the traveltime changes ($\langle \tau(t) \rangle = -\epsilon t$) using the stretching method [*Hadziioannou et al.*, 2009] for a given time window of the scattered waves, where ϵ is the stretching factor. The stretching factor is equal to the estimated fractional velocity change within the time window. To obtain the optimal stretch factor, we minimize

$$\min \quad f(\epsilon) = ||\hat{u}(t + \epsilon t) - u(t)||_2^{t, t_w}, \tag{2}$$

where $u(t)$ and $\hat{u}(t)$ are the original and the time-lapse coda signals, respectively.

The sensitivity kernel $K(\mathbf{s}, \mathbf{x_o}, \mathbf{r}, t)$ [*Planès et al.*, 2014], which depends on the source and receiver locations, the scattering property of the medium, and the traveltime of the scattered waves, is given by

$$K\left(\mathbf{s}, \mathbf{x_o}, \mathbf{r}, t\right) = \frac{\int_0^t P\left(\mathbf{s}, \mathbf{x_o}, t'\right) P\left(\mathbf{x_o}, \mathbf{r}, t - t'\right) \, dt'}{P(\mathbf{s}, \mathbf{r}, t)}, \tag{3}$$

where P is the normalized intensity of the scattered waves [*Pacheco and Snieder*, 2005]. The normalized intensity or the corresponding sensitivity kernel can be computed either by using analytical intensity models such as the diffusion intensity model or the radiative transfer intensity model [*Paasschens*, 1997]; or by using a numerical approach where the sensitivity kernel is computed by convolving numerically generated source and receiver intensity fields [*Kanu and Snieder*, 2014]. *Kanu and Snieder* [2014] show a comparison of the analytical and the numerical kernels using a statistically homogenous scattering model. For the imaging of localized changes in this study, we use the numerically generated sensitivity kernel. The intensity fields for the numerical kernel are computed from numerically simulated scattered wavefields excited at the source and the receiver locations. Using the numerically generated scattered intensity fields in equation (3), the sensitivity kernel $K(\mathbf{s}, \mathbf{x_o}, \mathbf{r}, t)$ is obtained for every given coda lapse time t. Figure 1 shows a numerical sensitivity kernel for the source-receiver pair (S-R) using a statistical homogeneous scattering velocity model. This sensitivity kernel corresponds to the scattered waves recorded at traveltime $t \simeq t^*$, where t^* is the mean free time. The recorded scattered waves at traveltime t results from the interference of scattered waves within the region bounded by the sensitivity kernel. The kernel shows high sensitivities at the source and receiver locations and
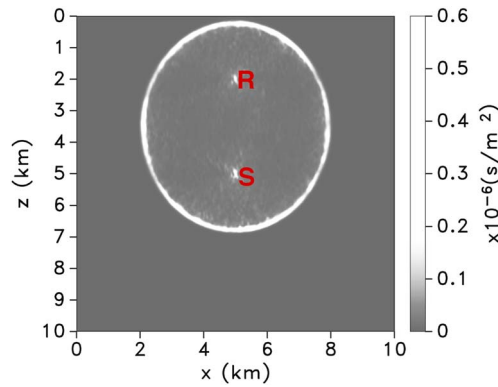
Figure 1. Sensitivity kernel $K(\mathbf{s}, \mathbf{x_o}, \mathbf{r}, t)$ for the source-receiver pair (S-R) within a statistical homogeneous scattering velocity model.

at the kernel front. The sensitivities at the source and receiver locations are predicted by [*Pacheco and Snieder*, 2005], while the sensitivity at the kernel front is a result of the convolution of the ballistic component of the scattered waves. Given an estimate of the statistical properties of the scattering model, the numerical solution of the sensitivity kernel gives the kernel for imaging the time-lapse changes present in a medium.

3. Multiple-Scattering-Induced Data Averaging

With increasing traveltime, due to multiple scattering of waves, the imaging data (the traveltime changes) spreads out in space and the sensitivity kernel for the time-lapse changes broadens spatially. Data averaging within time-lapse coda waves occurs because at increasing coda lapse time, the recorded coda results from the interference of scattered waves traveling across broader region of the scattering medium. To illustrate the effect of the spatial broadening of the multiply scattered waves on the distribution of the traveltime changes recorded on source-receiver pairs, we model, using finite-difference acoustic modeling, the traveltime changes due to a localized Gaussian velocity change (Figure 2, yellow arrow points to the location of the velocity change). Figure 3 shows an azimuthal dependence of estimated velocity changes due to a Gaussian positive velocity change within a statistical homogeneous model (Figure 2) using the circular receiver array and a source embedded in the middle of the model (Figure 2, blue dot). The azimuth of the Gaussian velocity change is along azimuth 90^0 (Figure 3, red line) with a radius of 0.5 km and a maximum velocity change of 1%. The scattering model is defined by the following von Karman parameters: exponent $\kappa = 0.5$, fractional fluctuation strength $\epsilon = 0.5$, correlation distances $a_z = a_x = 0.05$ km, an average velocity v_0 of 3.5 km/s, a grid spacing of 10 m-by-10 m, time sample of 0.001 s, and a dominate frequency of 15 Hz [*Sato et al.*, 2012]. We impose perfectly matched layer (PML) absorbing boundary conditions along the four sides of the velocity model. We assume acoustic waves generated by an explosive source thereby ignoring the effects of the source radiation and elastic wave modes.

We show the estimated velocity change for 36 source-receiver pairs at different azimuths for five coda lapse times. Figure 3 shows nonzero estimated velocity changes for source-receiver pairs with azimuth close to the azimuth of the Gaussian velocity change early in the coda ($t < t^*$). The mean free time (t^*) is given by

$$t^* = \frac{1}{v_0 g^*}, \tag{4}$$

where v_0 is the average velocity of the scattering model and g^* is the transfer scattering coefficient which in 2-D scattering von Karman medium is given by [*Saito et al.*, 2003; *Sato et al.*, 2012]

$$g^*(k_0) = 4k_0^3 \epsilon^2 a^2 \kappa \int_0^\pi \frac{1 - \cos\phi}{\left(1 + 4a^2 k_0^2 \sin^2(\phi/2)\right)^{\kappa+1}} \mathrm{d}\phi, \tag{5}$$

where ϕ is the scattering angle for the scattered waves of a wave number k_0.

In the coda time ($t > t^*$), the velocity change spreads to other source-receiver pairs far from the Gaussian velocity change. The estimated velocity
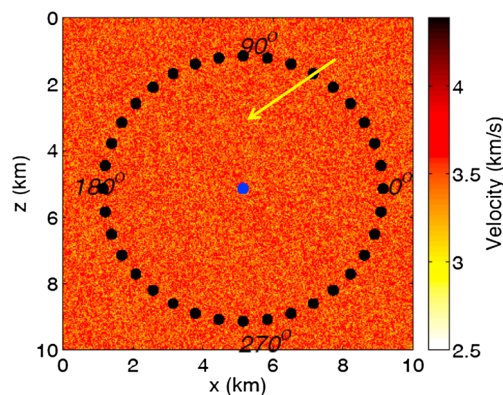

Figure 2. The model geometry used for data averaging test. A Gaussian velocity change is centered at location $[x, z] = [5, 3]$ km within a statistically homogeneous velocity model. The data averaging test uses a ring of receivers (black dots) and S source (blue dot) located at $[x, z] = [5, 5]$ km. The azimuth of the receivers is specified by the degrees. The yellow arrow points to the location of the velocity change.
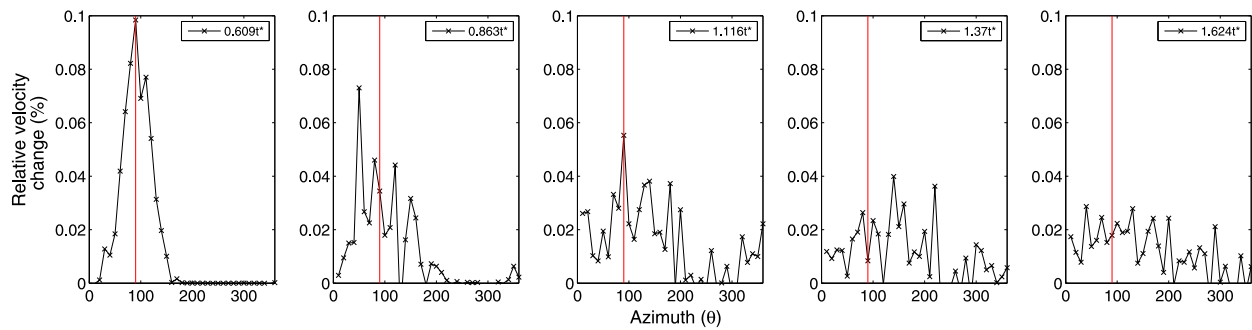
Figure 3. Azimuthal dependence of the estimated velocity change due to a Gaussian positive velocity change indicated with the yellow arrow in Figure 2 (lies at azimuth 90° (red line)). The figure panels are the estimated velocity changes at various coda lapse times measured by the transport mean free time t^* of the scattering model.

change becomes uniform across receivers at large coda lapse time ($t \gg t^*$). The estimated velocity changes are path-averaged velocity changes of all the interfering scattered waves recorded within the coda wave time window used to estimate the velocity changes. Given that the velocity change is localized, the estimated velocity change is a fraction of the true maximum velocity change in the medium.

4. Time-Lapse Imaging in Statistically Heterogenous Model

To explore imaging a localized velocity change within a statistically heterogeneous medium using the estimated traveltime change, we consider the geometry shown in Figure 4, which shows both the velocity (scattering) model and t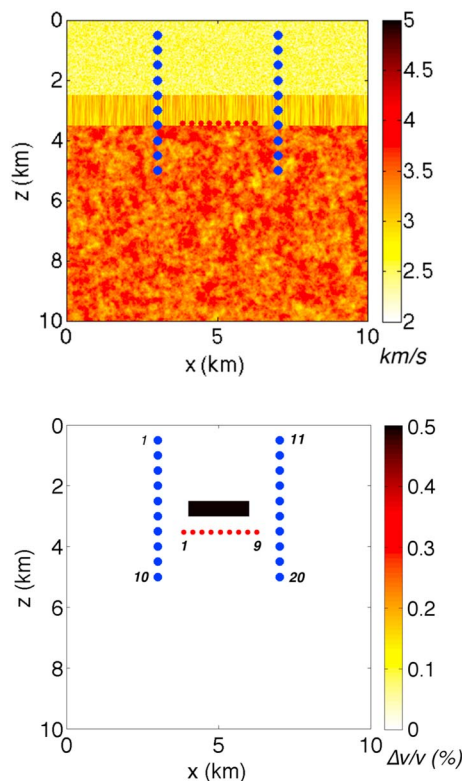he time-lapse velocity change for our imaging problem. The velocity model is a three-layer model, with each layer having scattering properties of different statistical characteristics. The statistical characteristics of the top and the bottom scattering layers are structurally isotropic, while the middle layer is statistically heterogeneous characterizing a highly fractured reservoir. The scattering properties of the layers have random heterogeneities defined by the 2-D von Karman power spectral density function. The von Karman parameters are as follows: for the top layer, $\kappa = 0.5, \epsilon = 0.1, a_z = a_x = 0.01$ km, and an average velocity v_0 of 2.0 km/s; for the bottom layer, $\kappa = 0.8$, $\epsilon = 0.1, a_z = a_x = 0.1$ km, and an average velocity v_0 of 3.5 km/s. The middle layer which mimics a vertically fractured reservoir is defined by the following von Karman parameters: $\kappa = 0.5, \epsilon = 0.1$, $a_z = 0.5$ km, $a_x = 0.0001$ km, and an average velocity v_0 of 3.0 km/s. The boundaries of the velocity model are extended to $[x_0, z_0] = [-10, -10]$ km and $[x_\infty, z_\infty] = [20, 20]$km to prevent waveform distortion due to the boundaries within the coda time windows used for imaging. We impose the PML-absorbing boundary conditions.

The time-lapse change is a +0.5% velocity change in the rectangle embedded within the middle layer shown in Figure 4 (bottom). To monitor and resolve this localized change, we use two vertical receiver arrays representing two boreholes located on opposite sides of the localized change. These

Figure 4. Numerical model for time-lapse inversion of localized positive velocity change with the used sources (red circles) and receivers (blue circles). (top) The reference velocity (scattering) model with the source-receiver setup; (bottom) the true localized velocity change (black rectangle) with the source-receiver setup.

boreholes record time-lapse scattered waves generated by nine sources that are located along a horizontal line. This source-receiver setup depicts time-lapse monitoring with repeating microseismic events whose scattered waves (codas) are recorded in the two boreholes. We assume acoustic waves generated by an explosive source; hence, we are not accounting for the effect of the nonisotropic source radiation and elastic wave modes.

4.1. Model and Data Resolution

For imaging of the time-lapse changes, the resolution of the imaged localized changes using multiply scattered waves depends on the traveltime of the scattered waves, the monitoring source-receiver array, and the scattering properties of the scattering model. To consider the resolution of the inverse problem, we consider both the model resolution and the data resolution. The model resolution considers the impact of the spatial broadening of the kernel on the resolution of the inverse solution, while the data resolution evaluates the effect of the data averaging.

Consider an inverse problem $\mathbf{d} = \mathbf{Km}$ (ignoring noise due either to data measurement or the model discretization), where $\mathbf{m}$ is the model, $\mathbf{d}$ is the data, and the $\mathbf{K}$ is a discretized version of the Frechet derivative which describes the sensitivity of the data to the model. We minimize the regularized least squares objective function ϕ:

$$\phi = ||(\mathbf{d} - \mathbf{K\,m})||_2^2 + \beta||\mathbf{m}||_2^2, \tag{6}$$

where β is the trade-off parameter. We determine the trade-off parameter using generalized cross validation [*Aster et al.*, 2013].

The estimated model is

$$\mathbf{m} = \left[\mathbf{K}^T\mathbf{K} + \beta\mathbf{I}\right]^{-1}\mathbf{K}^T\mathbf{K}\dot{\mathbf{m}}, \tag{7}$$

where $\dot{\mathbf{m}}$ is the actual model and $\mathbf{I}$ is an identity matrix. Equation (7) can be rewritten as follows:

$$\mathbf{m} = \mathbf{R}_m\dot{\mathbf{m}}, \tag{8}$$

where $\mathbf{R}_m = [\mathbf{K}^T\mathbf{K} + \beta\mathbf{I}]^{-1}\mathbf{K}^T\mathbf{K}$ is the model resolution matrix. The model resolution matrix $\mathbf{R}_m$ explains how the inverse solution is a smeared out version of the actual model $\dot{\mathbf{m}}$.

From equation (8),

$$\mathbf{m} = \mathbf{R}_m\dot{\mathbf{m}} = \sum_{i=1}^{N}\tilde{m}_i\mathbf{p}^i \tag{9}$$

where N is the dimension of the model and $\mathbf{p}^i$ are the column vectors of the model resolution matrix $\mathbf{R}_m$. The $\mathbf{p}^i$ vectors which are usually called the point spread functions, explain how the ith element of the actual model is mapped to the estimated model. Following *Oldenborger and Routh* [2009], we can determine how well an ith parameter of the model is resolved by solving

$$\left[\mathbf{K}^T\mathbf{K} + \beta\mathbf{I}\right]\mathbf{p}^i = \mathbf{K}^T\mathbf{K}\Delta_\mathbf{i} \tag{10}$$

for $\mathbf{p}^i$ using a delta function vector $\Delta_\mathbf{i}$ which has 1 at the ith vector element and zeros elsewhere. To solve for $\mathbf{p}^i$, we use a linear conjugate gradient algorithm. Each of the $\mathbf{p}^i$ are obtained after five iterations. We compare the model resolution at various time windows of the multiply scattered waves (coda). To estimate the traveltime changes across the coda, we use 0.6 s time windows with each window overlapping 0.1 s with the previous time window. Each time window contains about 10 cycles of the signal, and the windowed signals are tapered with a Tukey time window [*Snieder et al.*, 2002]. To get more data points for the inversion, we interpolate estimated traveltime changes from time interval 0.5 s to 0.02 s. To evaluate the model resolution across the coda, we consider two time window categories. These window categories define time windows that contain sub-time windows. Category 1 uses a 0.55 s time window with progressive shifts of the centertime of the window to later coda times by 0.5 s (Figure 5, top). For Category 2, each of the time windows start from 0.30 s before the first arrival. The first time window (Figure 5, black rectangle) extends to 0.25 s after the first arrival.
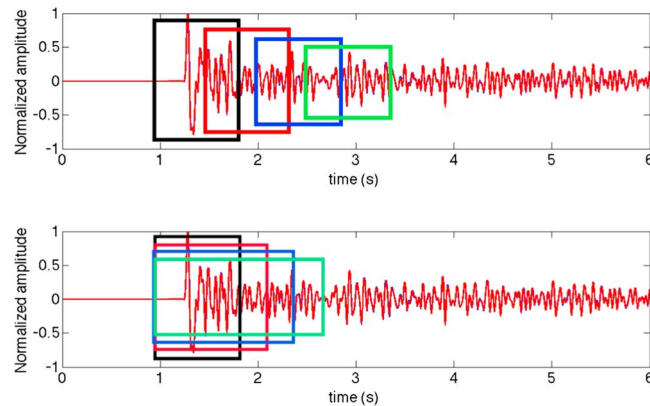
Figure 5. The coda time windows used for the time-lapse imaging. (top) The used time windows for Category 1 resolution analysis and imaging; (bottom) the used time windows for Category 2 resolution analysis and imaging. The time-lapse signals are signals generated by source 5 and recorded on receiver 2.

The extent of the rest of the time windows increases by 0.25 s (Figure 5, bottom), i.e., extending to 0.80 s, 1.05 s, and 1.30 s, respectively, after the traveltime of the first arrival.

Figure 6 (top row) shows the $\mathbf{p}^i$ for the model elements located at $[x, z] = [5, 3]$ km for the coda time windows in Figure 5 (top). This model element corresponds to the model location inside the middle horizon which is between z of 2.5–3.5 km (Figure 4). The resolved point spread functions suggest a decrease of the model resolution with increased centertime of the time window (Figure 6). This reduced resolution results from the spatial broadening of the sensitivity kernel. However, using the coda time windows in Figure 5 (bottom), the velocity change $\mathbf{p}^i$ is better resolved with increasing centertime of the time window (Figure 6, bottom row). Extending the time windows to longer coda lapse time in Category 2 (Figure 5, bottom), we incorporate additional model information into the inverse process which helps to improve model resolution (Figure 6, bottom row).

Due to multiple scattering of the waves within the scattering model, the estimated traveltime change is a weighted average of the traveltime change across the scattered trajectory within the scattering medium [*Snieder*, 2006]. Figure 7 shows the average estimated fractional velocity change across the time windows for Categories 1 and 2, as defined in Figure 5. These values are the average values of the subwindows in the time windows shown in the categories. The receiver and the source numbering in Figure 7 are shown in Figure 4. In Figure 7 (top row), the average estimated velocity changes are smeared across the source-receiver pairs
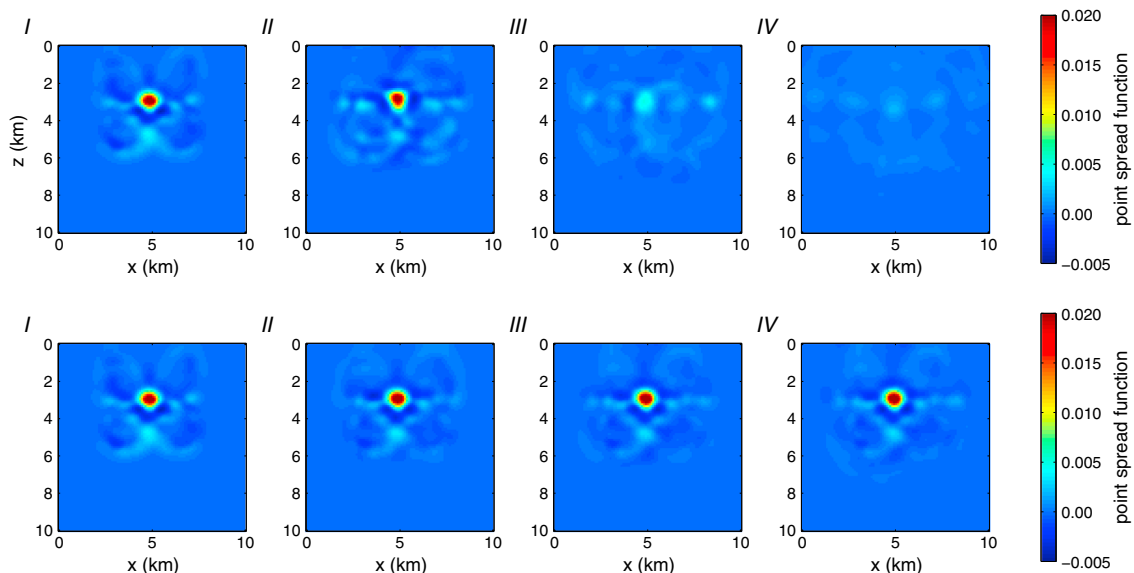

Figure 6. The point spread function $\mathbf{p}^i$ for the inverted model at $[x, z] = [5, 3]$ km using the (top row) Category 1 and (bottom row) Category 2 time windows. The point spread function $\mathbf{p}^i$ uses time windows: I (black window), II (red window), III (blue window), and IV (green window) in Figure 5.
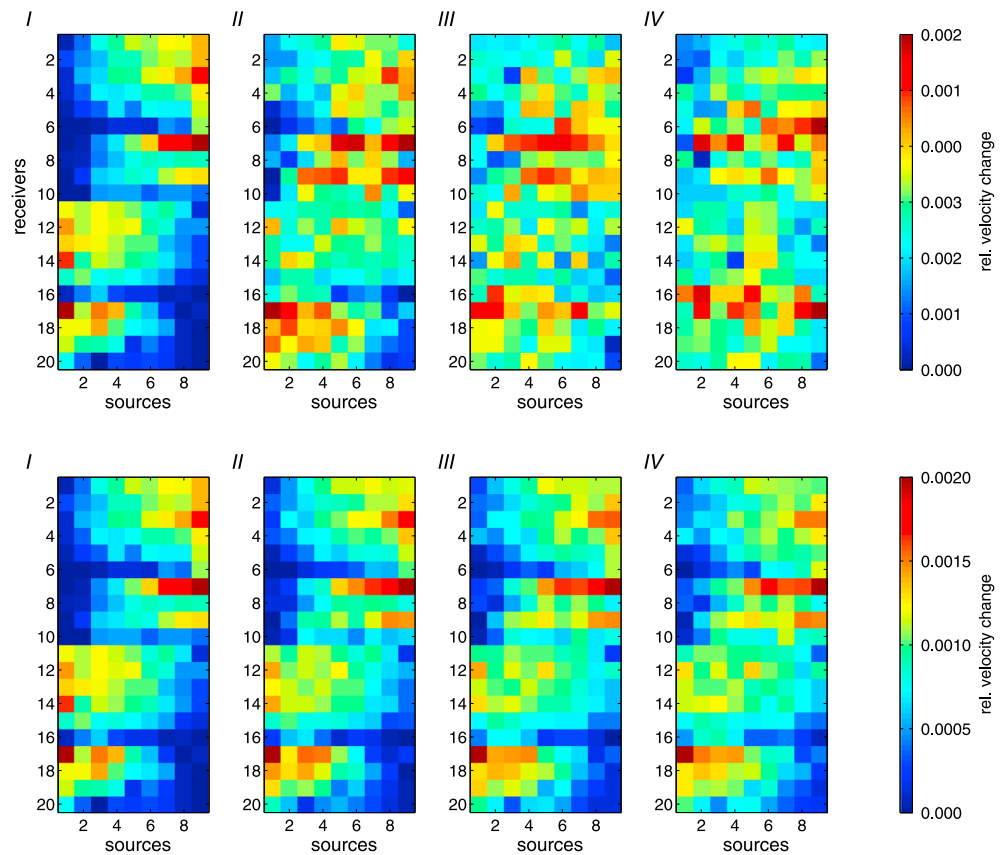
Figure 7. Data spread function for the inverted model using the (top row) Category 1 time windows and (bottom row) Category 2 time windows. Each value is an estimated fractional velocity change for a given source-receiver pair.

with increasing the centertime of the coda waves. The smearing of the estimated velocity changes means that there are smaller or insignificant differences between the estimated velocity changes for source-receiver lines across the location of the change and the estimated velocity changes for source-receiver lines away from the location of the change (Figure 7, top row). Also, due to the averaging of the estimated velocity changes due to multiple scattering, the estimated velocity change is a fraction of the true maximum velocity change in the medium (explained in Figure 3). In Category 2, the smearing of the estimated velocity change is smaller than in Category 1. In Category 2, the average velocity change for all the time windows contains the estimates of the velocity change from the direct or forward scattered waves.

4.2. Time-Lapse Inversion Using Numerical Sensitivity Kernel

To localize the weak velocity change in Figure 4, we minimize the objective function ϕ (equation (6)). The objective function ϕ corresponds to solving the following least squares problem:

$$\mathbf{K}^T \mathbf{d} = \left[\mathbf{K}^T \mathbf{K} + \beta \mathbf{I} \right] \mathbf{m}, \tag{11}$$

where $\mathbf{d}$ is the estimated traveltime change δt and $\mathbf{m}$ is the fractional velocity change. To solve equation (11), we use a linear conjugate gradient method. All the imaged velocity changes in this section are obtained after five iterations.

The inverted velocity images recover the location of the velocity change, albeit with some artifacts. For the time windows shown in Figure 5 (bottom) (Category 2 time windows), the resolution of the inverted velocity change varies with different coda time windows. Figure 8 (top) shows the temporal stacked sensitivity kernel (equation (12)) for each time window in Figure 5 (bottom).

$$\hat{K}\left(\mathbf{s}, \mathbf{x_o}, \mathbf{r}\right) = \sum_{t=t_1}^{t=t_2} K\left(\mathbf{s}, \mathbf{x_o}, \mathbf{r}, t\right), \tag{12}$$

where t_1 and t_2 are the start and end times of the time window used for inversion.
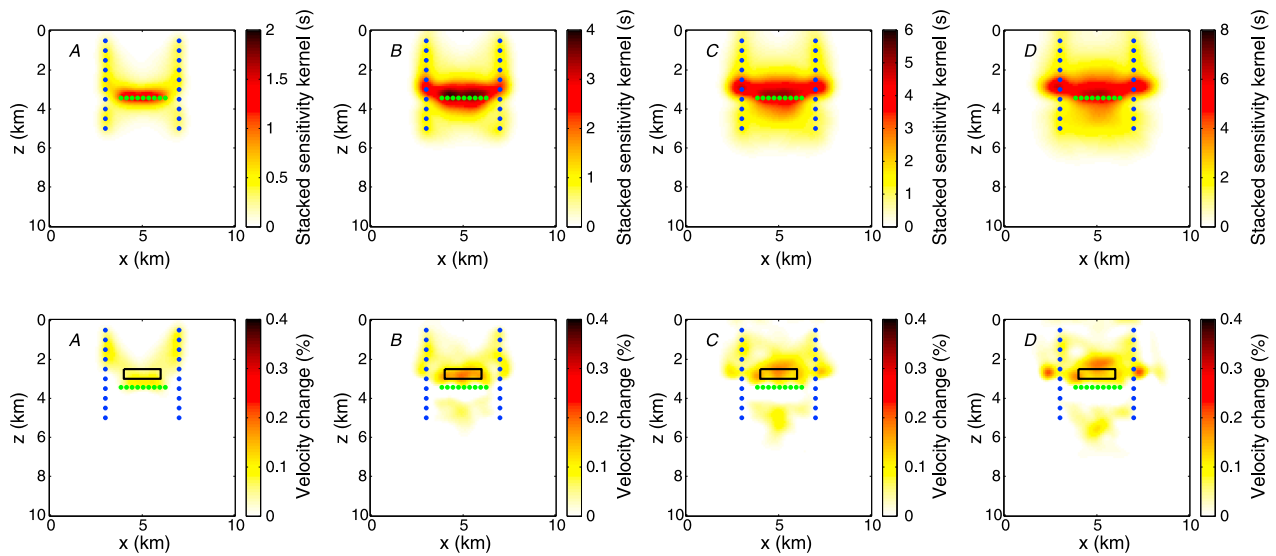
Figure 8. Temporal stack of the (top row) numerical sensitivity kernel of all the source-receiver pairs used for inversion of the (bottom row) velocity change. Inverted fractional velocity change uses the coda time windows in Figure 5 (bottom) for (a) with black time window, (b) with red time window, (c) with blue time window, and (d) with green time window. The black box shows the extent of the velocity change.

The stacked sensitivity kernels show relatively high sensitivities at the source locations which are enhanced by the close proximity of the sources and the strong scattering within the middle layer of the model. Figure 8 (bottom row) shows the inverted velocity changes with the corresponding time windows. Figure 8b provides the best resolved and localized image of the velocity change. In Figure 8a, the inferred velocity change is negligible because of relatively low sensitivity of scattered within the corresponding time window on the
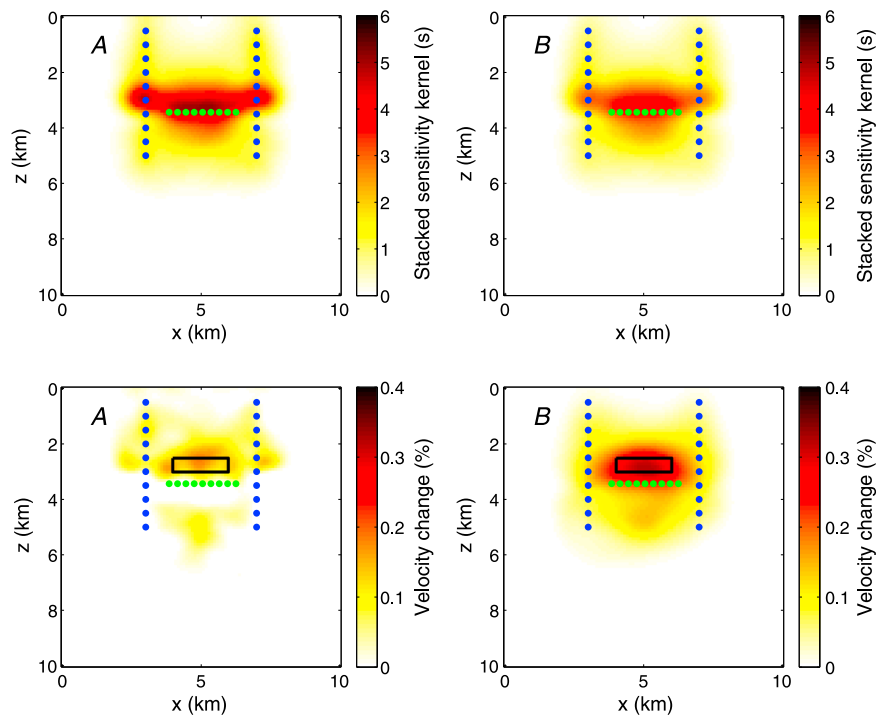

Figure 9. Suppression of localized high sensitivities in the numerical sensitivity kernel. Temporal stack of the (top row) sensitivity kernel of all the source-receiver pairs used for inversion of the localized (bottom row) velocity change. Inverted fractional velocity change uses the coda time window in the blue time window in Figure 5 (bottom). (a) Kernel with unsuppressed source sensitivity; (b) kernel with suppressed source sensitivity.
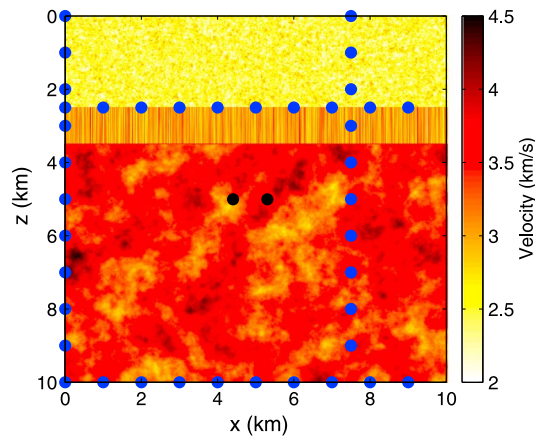
Figure 10. Distribution of the sources (black dots) and receivers (blue dots) used for estimating the effective mean free path l of the heterogeneous scattering model.

velocity change. At later times (Figures 8c and 8d), there is a shift of the imaged velocity change from the true position. This shift is due to the localized high sensitivities in the sensitivity kernel present at the source, receiver, and kernel front locations [*Kanu and Snieder*, 2014]. The impact of the high sensitivities at the source location is enhanced by the clustering of the sources. For a dispersed source, the stacked sensitivity will be lower. Figure 9 shows the effect of reducing the relatively high sensitivity at the source location for the blue time window (Figure 5). With the reduction of the relatively high source sensitivities close to the background sensitivity (clipping the source sensitivity to the L_2 norm of the spatial kernel at each time sample), we correct the shift in the imaged velocity change. The amount of suppression of the source sensitivity we applied here is obtained after a couple of tries. The optimal amount of suppression that will be needed will vary with the source-receiver geometry and the scattering properties around the sources and receivers.

4.3. Time-Lapse Inversion Using Analytical Sensitivity Kernel

Current methods for imaging localized changes within heterogenous medium using coda waves assumes statistical homogeneity of the scattering medium [*Obermann et al.*, 2013a]. The imaging involves computing the sensitivity kernel with analytical models of the scattered intensity such as diffusion or radiative transfer intensity models. In this section, we invert the time-lapse velocity change in Figure 4 using the radiative transfer-based sensitivity kernel.

To compute the analytical sensitivity kernel, we approximate the scattered intensity using infinite 2-D radiative transfer intensity model [*Paasschens*, 1997] defined by an effective mean free path length l. The 2-D radiative transfer intensity model is given by

$$P(\mathbf{s}, \mathbf{r}, t) = \frac{\exp(-v_0 t/l)}{2\pi R_{sr}} \delta(v_0 t - R_{sr}) + \frac{1}{2\pi l v_0 t} \left(1 - R_{sr}^2/v_0^2 t^2\right)^{-1/2} \times \exp\left(\sqrt{v_0^2 t^2 - R_{sr}^2}/l - v_0 t\right) \Theta(v_0 t - R_{sr}), \quad (13)$$

where R_{sr} is the source-receiver distance, t is the traveltime of the scattered intensity, v_0 is the average velocity of the scattering medium, δ is the delta function, and Θ is the Heaviside step function.

We estimate the scattering mean free path length l from the coherent part $\langle \phi(t) \rangle$ of the scattered waveform [*Obermann et al.*, 2013b]. Using 40-receiver rectangu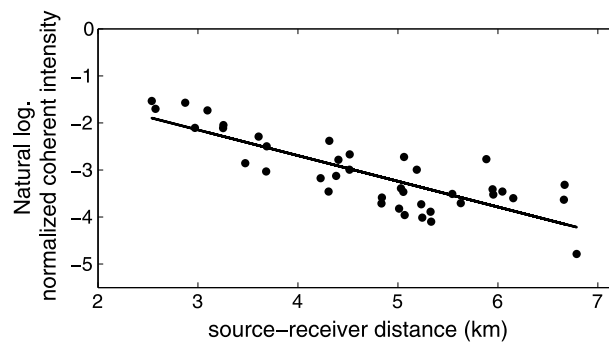lar array within the scattering model in Figure 10 surrounding two sources at locations $[x, y] = [4.5, 5.0]$ km and $[x, y] = [5.5, 5.0]$ km and 30 realizations of the scattering model in Figure 4, we simulate the coherent part $\langle \phi(t) \rangle$ of the scattered waveform, where $\langle \dots \rangle$ is an ensemble average across the model realizations. The power spectrum of the coherent scattered waveform, after correcting for geometrical spreading, $|\langle \Phi(\omega) \rangle|$ is given by

Figure 11. Distribution of the normalized coherent intensity with source-receiver distances R_{sr}. The coherent intensity is averaged over 30 realizations of the scattering model in Figure 4. The inverse of the slope of the line fit gives the estimate of the effective mean free path l.

$$|\langle \Phi(\omega) \rangle|^2 = \exp\left(-\frac{R_{sr}}{l}\right), \quad (14)$$

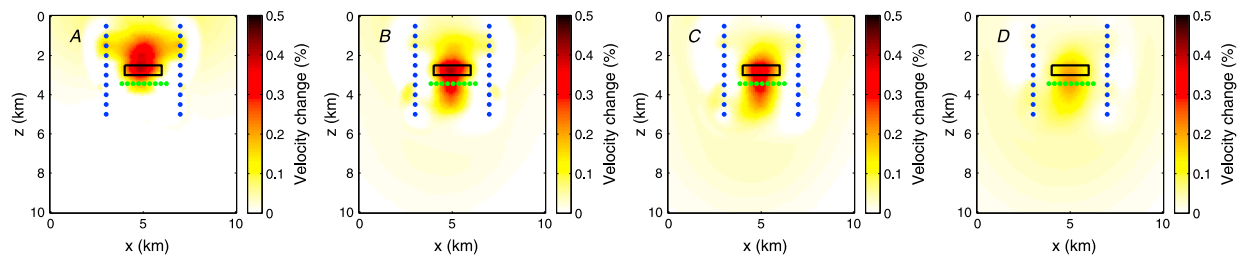where R_{sr} is the source-receiver distance.

Figure 12. Inverted fractional velocity change using the coda time windows in Figure 5(bottom) for (a) with black time window, (b) with red time window, (c) with blue time window, and (d) with green time window, using analytical sensitivity kernel. The black box shows the extent of the velocity change.

Figure 11 shows the distribution of the coherent energy versus the source-receiver distances after correcting for geometrical spreading. Using the inverse slope of the regression line (Figure 11), the effective scattering mean free path length l is 1.83 ± 0.44 km.

Figure 12 shows the inverted velocity change using the radiative transfer-based sensitivity kernel defined by the estimated scattering mean free path length l. We solve the same inverse problem described in section 4.2. The only difference between the inverse problem in sections 4.2 and 4.3 lies on the kernel used for inverting the localized velocity change. With the time windows in Figure 5, we image the correct location of the localized velocity change in Figure 4. However, in Figure 12 the shape of the velocity change is less resolved with the analytical kernel compared to the imaged change using the numerical kernel in Figure 9. The weak resolution on the shape of the velocity change results from the homogeneity assumption of the analytical kernel and also on the source-receiver configuration used. The two vertical receiver arrays used provide weak vertical resolution on the imaged velocity change.

5. Conclusions

We demonstrate the capability of resolving localized weak changes within heterogeneous scattering media using multiply scattered waves. Our imaging algorithm builds on the work of *Pacheco and Snieder* [2005] and *Rossetto et al.* [2011]. Using estimated time-lapse traveltime change, we demonstrate with a numerical example how well we can localize a weak velocity change within a heterogeneous three-layer scattering model. We image the localized velocity change in the three-layer model without assuming any statistical homogeneity of the scattering model. For this model, our imaging recipe which uses numerically generated sensitivity kernels, resolves the location of the velocity change especially early in the coda wave. Comparison of the imaged localized change using numerical kernel with the imaged solution of the analytical kernel suggests that numerical kernel provides a stronger constraint of the shape of the imaged velocity change, because the numerical incorporates the local statistical properties of the scattering model. To gain the advantage of the numerical kernel when working with real data, the numerical kernel needs to be computed with a prior model that explains the statistical properties of the scattering medium monitored.

The resolution of the imaged velocity change progressively decreases with increasing traveltime of the coda waves we use for the imaging. The decrease in the resolution of the velocity change results from the spatial broadening of the sensitivity kernel with traveltime and the averaging out of the estimated changes across the sources and receivers. An effective resolution of the localized velocity change will involve a joint inversion of the time-lapse changes estimated across the coda lapse time [*Pacheco and Snieder*, 2005; *Obermann et al.*, 2014].

References

Aster, R. C., B. Borchers, and C. H. Thurber (2013), *Parameter Estimation and Inverse Problems*, Academic Press, Waltham, Mass.

Belkebir, K., P. C. Chaumet, and A. Sentenac (2006), Influence of multiple scattering on three-dimensional imaging with optical diffraction tomography, *J. Opt. Soc. Am. A*, *23*(3), 586–595, doi:10.1364/JOSAA.23.000586.

Cowan, M. L., I. P. Jones, J. H. Page, and D. A. Weitz (2002), Diffusing acoustic wave spectroscopy, *Phys. Rev. E*, *65*, 066605.

Daley, T., L. Myer, J. Peterson, E. Majer, and G. Hoversten (2008), Time-lapse Crosswell seismic and VSP monitoring of injected CO_2 in a brine aquifer, *Environ. Geol.*, *54*(8), 1657–1665, doi:10.1007/s00254-007-0943-z.

Gaburro, R., C. J. Nolan, T. Dowling, and M. Cheney (2007), Imaging from multiply scattered waves, in *Proc. of SPIE, Medical Imaging 2007: Ultrasonic Imaging and Signal Processing*, vol. 6513, edited by S. Y. Emelianov and S. A. McAleavey, pp. 304–311, SPIE, San Diego, Calif., doi:10.1117/12.712569.

Grêt, A., R. Snieder, and U. Özbay (2006), Monitoring in situ stress changes in a mining environment with coda wave interferometry, *Geophys. J. Int.*, *167*(2), 504–508, doi:10.1111/j.1365-246X.2006.03097.x.

Hadziioannou, C., E. Larose, O. Coutant, P. Roux, and M. Campillo (2009), Stability of monitoring weak changes in multiply scattering media with ambient noise correlation: Laboratory experiments, *J. Acoust. Soc. Am.*, *125*(6), 3688–3695, doi:10.1121/1.3125345.

Kanu, C., and R. Snieder (2014), Numerical computation of the sensitivity kernel for time-lapse monitoring with multiply scattered waves, *Center for Wave Phenomena Rep. 816*, pp. 291–306, Fed. Inst. for Mater. Res. and Test., Berlin.

Landrø, M. (2001), Discrimination between pressure and fluid saturation changes from time-lapse seismic data, *Geophysics*, *66*(3), 836–844, doi:10.1190/1.1444973.

Larose, E., and S. Hall (2009), Monitoring stress related velocity variation in concrete with a 2×10^{-5} relative resolution using diffuse ultrasound, *J. Acoust. Soc. Am.*, *125*(4), 1853–1856, doi:10.1121/1.3079771.

Larose, E., T. Planes, V. Rossetto, and L. Margerin (2010), Locating a small change in a multiple scattering environment, *Appl. Phys. Lett.*, *96*(20), 204101, doi:10.1063/1.3431269.

Lumley, D. E. (2001), Time-lapse seismic reservoir monitoring, *Geophysics*, *66*(1), 50–53, doi:10.1190/1.1444921.

Nishimura, T., N. Uchida, H. Sato, M. Ohtake, S. Tanaka, and H. Hamaguchi (2000), Temporal changes of the crustal structure associated with the M6.1 earthquake on September 3, 1998, and the volcanic activity of Mount Iwate, Japan, *Geophys. Res. Lett.*, *27*(2), 269–272, doi:10.1029/1999GL005439.

Nolet, G. (1987), *Seismic Tomography: With Applications in Global Seismology and Exploration Geophysics*, Springer, Netherlands.

Obermann, A., T. Planès, E. Larose, and M. Campillo (2013a), Imaging pre-eruptive and co-eruptive structural and mechanical changes of a volcano with ambient seismic noise, *J. Geophys. Res. Solid Earth*, *118*, 6285–6294, doi:10.1002/2013JB010399.

Obermann, A., T. Planès, E. Larose, C. Sens-Schönfelder, and M. Campillo (2013b), Depth sensitivity of seismic coda waves to velocity perturbations in an elastic heterogeneous medium, *Geophys. J. Int.*, *194*(1), 372–382.

Obermann, A., B. Froment, M. Campillo, E. Larose, T. Planès, B. Valette, J. Chen, and Q. Liu (2014), Seismic noise correlations to image structural and mechanical changes associated with the M_w 7.9 2008 Wenchuan earthquake, *J. Geophys. Res. Solid Earth*, *119*, 3155–3168, doi:10.1002/2013JB010932.

Oldenborger, G. A., and P. S. Routh (2009), The point-spread function measure of resolution for the 3-D electrical resistivity experiment, *Geophys. J. Int.*, *176*(2), 405–414.

Paasschens, J. C. J. (1997), Solution of the time-dependent Boltzmann equation, *Phys. Rev. E*, *56*(1), 1135–1141, doi:10.1103/PhysRevE.56.1135.

Pacheco, C., and R. Snieder (2005), Time-lapse travel time change of multiply scattered acoustic waves, *J. Acoust. Soc. Am.*, *118*(3), 1300–1310, doi:10.1121/1.2000827.

Pine, D. J., D. A. Weitz, P. M. Chaikin, and E. Herbolzheimer (1988), Diffusing wave spectroscopy, *Phys. Rev. Lett.*, *60*(12), 1134–1137, doi:10.1103/PhysRevLett.60.1134.

Planès, T., E. Larose, L. Margerin, V. Rossetto, and C. Sens-Schönfelder (2014), Decorrelation and phase-shift of coda waves induced by local changes: Multiple scattering approach and numerical validation, *Waves Random Complex Medium*, *24*, 99–125, doi:10.1080/17455030.2014.880821.

Poupinet, G., W. L. Ellsworth, and J. Frechet (1984), Monitoring velocity variations in the crust using earthquake doublets: An application to the Calaveras fault, California, *J. Geophys. Res.*, *89*(B7), 5719–5731, doi:10.1029/JB089iB07p05719.

Rossetto, V., L. Margerin, T. Planès, and E. Larose (2011), Locating a weak change using diffuse waves: Theoretical approach and inversion procedure, *J. Appl. Phys.*, *109*(3), 903–911, doi:10.1063/1.3544503.

Saito, T., H. Sato, M. Fehler, and M. Ohtake (2003), Simulating the envelope of scalar waves in 2d random media having power-law spectra of velocity fluctuation, *Bull. Seismol. Soc. Am.*, *93*(1), 240–252.

Sato, H., M. C. Fehler, and T. Maeda (2012), *Seismic Wave Propagation and Scattering in the Heterogeneous Earth: Second Edition*, Springer, Berlin.

Snieder, R. (2006), The theory of coda wave interferometry, *Pure Appl. Geophys.*, *163*(2–3), 455–473, doi:10.1007/s00024-005-0026-6.

Snieder, R., A. Grêt, H. Douma, and J. Scales (2002), Coda wave interferometry for estimating nonlinear behavior in seismic velocity, *Science*, *295*(5563), 2253–2255, doi:10.1126/science.1070015.

Wegler, U., and C. Sens-Schönfelder (2007), Fault zone monitoring with passive image interferometry, *Geophys. J. Int.*, *168*(3), 1029–1033, doi:10.1111/j.1365-246X.2006.03284.x.